Polarity Dependent Electrowetting for Directional Transport of Water through Patterned Superhydrophobic Laser Induced Graphene Fibers

Journal Pre-proof

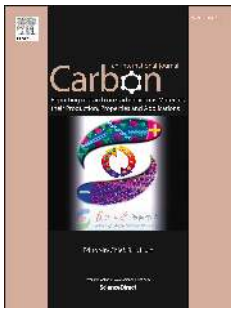

Polarity Dependent Electrowetting for Directional Transport of Water through Patterned Superhydrophobic Laser Induced Graphene Fibers

Sujit Deshmukh, Debosmita Banerjee, Juan Sebastian Marin Quintero, Sam J. Fishlock, James McLaughlin, Prashant R. Waghmare, Susanta Sinha Roy

PII: S0008-6223(21)00620-5

DOI: https://doi.org/10.1016/j.carbon.2021.06.033

Reference: CARBON 16394

To appear in: *Carbon*

Received Date: 8 April 2021

Revised Date: 25 May 2021

Accepted Date: 7 June 2021

Please cite this article as: S. Deshmukh, D. Banerjee, J.S. Marin Quintero, S.J. Fishlock, J. McLaughlin, P.R. Waghmare, S.S. Roy, Polarity Dependent Electrowetting for Directional Transport of Water through Patterned Superhydrophobic Laser Induced Graphene Fibers, *Carbon*, https://doi.org/10.1016/j.carbon.2021.06.033.

Sujit Deshmukh (S. D.), Prashant R. Waghmare., Susanta Sinha Roy, conceived the idea, contributed to design the experimental studies, and wrote the manuscript. S. D. and Sam J. Fishlock contributed to the synthesis of LIG films. S. D. and Juan Sebastian Marin Quintero performed the electrowetting experiments. S. D. and Debosmita Banerjee carried out materials characterization experiments. All authors contributed to scientific discussions of the results. All authors reviewed the manuscript.

Graphical Abstract

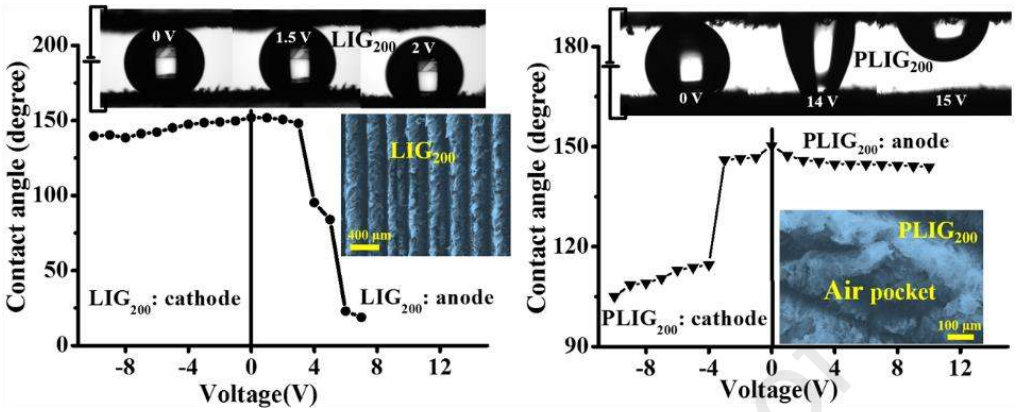

Polarity Dependent Electrowetting for Directional Transport of Water through Patterned Superhydrophobic Laser Induced Graphene Fibers

Sujit Deshmukh[1, 3], Debosmita Banerjee[1], Juan Sebastian Marin Quintero[3], Sam J. Fishlock[2], James McLaughlin[2], Prashant R. Waghmare [3]*, Susanta Sinha Roy [1]*

[1]*Department of Physics, School of Natural Sciences, Shiv Nadar University, NH-91, Greater Noida, Uttar Pradesh 201314, India*

[2]*Nanotechnology and Integrated Bioengineering Centre, University of Ulster, Jordanstown Campus, Newtownabbey, Northern Ireland BT37 0QB U.K.*

[3]*Interfacial Science and Surface Engineering Lab (iSSELab), Department of Mechanical Engineering, University of Alberta, Edmonton, Alberta T6G2G8, Canada*

1

[1] *Corresponding authors E-mail: waghmare@ualberta.ca and susanta.roy@snu.edu.in

Abstract

The possibilities of the precise control of wetting properties of a series of laser-induced graphene (LIG) films consisting of microscale air pockets on top of nano-scale surface roughness using electrowetting are demonstrated. By application of a marginal DC bias (~2 V), water can efficiently wet as well as can be pumped through the superhydrophobic LIG substrates. Interestingly, the electrowetting phenomenon is strongly dependent on the applied voltage polarity and it causes an abrupt wetting transition from superhydrophobic (contact angle ~152^{o}) Cassie state to superhydrophilic (contact angle ~7^{o}) Wenzel state on the LIG films. By analyzing the voltage polarity dependent electrowetting results with an equivalent electrical circuit model at the solid-liquid interface, and considering the hierarchical dual surface roughness (micro-nano scale), the transition between the "slippy" Cassie state and the "sticky" Wenzel states is explained. Furthermore, we demonstrate that the unique structural characteristics of the custom-designed micropatterned LIGs, with precisely tailored surface energy by simple post-annealing treatment, enable easy preparation of superhydrophobic LIG films. The approach to prepare stable superhydrophobic LIG with voltage polarity dependent wetting mode transition is used here to controllably transport of water through 3D porous LIG surfaces.

Keywords

Electrowetting; Laser-induced graphene; Micropatterned; Superhydrophobic; Superhydrophilic; Water transport

1. Introduction

In recent years, wettability control and capillary transport of water through carbon membranes have generated considerable interest, especially in the biomedical field where water flows

through biological water channels.[1][2] In general, the wettability of the solid surface is strongly prejudiced by either altering the surface chemistry or by introducing multiscale physical roughness.[3] Several experimental or theoretical studies have been adopted to exploit the surface roughness (both microscale and nanoscale roughness features) to engineer superhydrophobicity (Cassie state) or superhydrophilicity (Wenzel state).[3] These artificial synthesized surfaces maintain their wettability characteristics over a period of time but do not actively regulate their wettability after being prepared. It has been a real challenge to tune the wettability on demand, which can be solved by mimicking the electrowetting scenario where an external perturbation in the form of an electric field is accountable for the wettability variation from superhydrophobic to superhydrophilic state.[4],[5] The ability to real-time droplet actuation on a solid substrate using an electric field makes electrowetting suitable for many optical, biomedical, and electronics applications that have led to the commercially available liquid lenses and digital microfluidics diagnostics kits.[6–10] There is, therefore, renewed interest to synthesize a new material with a single-step process that is not only accessible for variable wettability but also adequate for electrowetting.

Graphene, the thinnest nanomaterial known so far, where carbon atoms packed into a 2D honeycomb lattice has gained huge recognition due to its fascinating electrical, thermal, and mechanical properties.[11–14] An often desired alteration of graphene wettability in the range of superhydrophobic to superhydrophilic includes specific approaches, such as controlling the relative proportion of electrolytes in graphene dispersed solvent, preparing graphene/carbon nanotube hybrids, introducing fluorine groups in the graphene sheet, functionalizing the graphene nanostructures.[3,15–19] Yet, in all the reported methods, multiple steps are involved to yield the desired surface functionalities and all the modifications are done in post-graphene formation. Moreover, the lack of large-scale production methods and translating these properties into an ordered architecture has been the main hurdle to use it in a practical application.

Recently the graphene-based 3D porous nanomaterial called laser-induced graphene (LIG), prepared from flexible polyimide (PI) sheets has been investigated worldwide due to its easy and scalable synthesis.[20–23] Its physical properties can be controlled by varying experimental conditions such as laser pulse parameters, laser power, and lasing atmosphere.[24,25] Applications of LIG for microsupercapacitors, electrochemical sensors, electrochemical water splitting, electrocatalysis, water treatment have been demonstrated where wettability control was the prime factor for improved device performances.[20–23],[26] LIG has now emerged as a smart material in which many commercial applications can be envisioned. Reports are available demonstrating that the wetting properties of LIG can be altered by preparing it under a controlled gas atmosphere.[24,25] However the method requires an additional controlled atmosphere chamber which reducing the advantage of LIG formation of being a simple and rapid process. Alternatively, a simple and superior electrowetting approach, by means of an external electric field can modulate the wettability of carbon-based films from superhydrophobic to superhydrophilic state.[27][28] In general, electrowetting refers to electrowetting on dielectrics (EWOD) where the electrowetting phenomenon is independent of the applied voltage polarity and contact angle responses with voltage are symmetrical in both positive and negative applied bias.[4] However, recently few studies have described the dielectric-free approach to electrowetting on the basal plane of conductive graphite surface where specific interactions at the water-graphite interface and graphite crystallinity are said to be responsible for electrowetting on conductive graphite and the phenomena is also referred to as electrically driven flow.[29–31] But surprisingly, until now, single-step synthesis of micropatterned LIG has not been investigated and no reports are available showing their electrowetting and corresponding wetting properties. Liquid repellency and electrowetting characteristics of hierarchical structured LIG fibers are still unexplored. It is well known that the introduction of hierarchical roughness is beneficial to produce stable hydrophobic surfaces and as compared with 2D and 3D carbon geometry,

carbon fibers with their flexible geometry are more suitable for multifunctional application.[32,33] Therefore, we believe the development of electrowettable superhydrophobic micropatterned LIG fibers in terms of the cost-effective simple production process could be of great significance in the field of surface science and engineering.

Aiming to expand the range of properties for LIG, in particular, to tune the underlying wettability of LIG surface, and eventually to further broaden the LIGs field of applications using electrowetting, here we presented polarity dependent low voltage electrowetting for electrically driven transport of water and precise actuation of droplets on LIG surfaces which are made of densely packed vertically aligned carbon nanofibers. Moreover, we report here a method to prepare LIG fiber and patterned LIG (PLIG) fiber under an ambient atmosphere where superhydrophobic LIG and PLIG fibers are obtained by post-annealing treatment and superhydrophilic LIG and PLIG fibers are obtained by mimicking the electrowetting scenario. Here we developed graphene walls where sequential air pockets are regularly distributed on the PLIG surface. Such a system can be considered as a two-scale structure; the regularly distributed micron size air pockets represent microscale surface roughness which is coupled with the nanoscale surface roughness associated with the sharp fiber tips. The influence of micropatterning, surface chemical functionalities, microstructure on the variable wettability, and corresponding electrowetting is investigated using scanning electron microscopy (SEM), X-ray photoelectron spectroscopy (XPS), transmission electron microscopy (TEM), and Raman spectroscopy. Finally, polarity dependent electrowetting characteristics are explained by analyzing the electrowetting behavior at the electrode/electrolyte interface with an equivalent circuit model (electrochemical impedance spectroscopy) and by taking into account the role of interfacial capacitance using cyclic voltammetry method.

2. Experimental Section

LIG fabrication

Unless otherwise indicated, polyimide sheets (PI, 0.005 inches) were used as received. A CO_2 laser cutter system (UniversalX-660 laser cutter platform) with a 10.6 μm laser wavelength was used for laser scribing on polymer sheets. The size of the laser beam is about 100 mm. Laser power at 10 W was maintained constant during laser scribing. The laser system also offers an option to set the pulses per inch (PPI) with a range of 10-1,000 PPI. We set the PPI value of 500 in our experiment. All laser experiments were carried out under environmental conditions. Prior to create air pockets, a crosshatch pattern with dimensions 400 × 200 μM is created using SOLIDWORKS software and then the pattern is printed on the PI sheet during the laser rastering process. Additionally, prepared LIG and patterned LIG are further air annealed at 200^{o}C for one hour. The grown samples are designated as LIG (laser-induced graphene fiber), PLIG (patterned LIG), LIG_{200}, and $PLIG_{200}$ (air annealed LIG and PLIG at 200^{o}C for one hour).

Material characterization

The surface morphology of the LIG films was characterized using Zeiss Sigma FESEM w/ EDX & EBSD scanning electron microscope (SEM). The height profiles of the graphene walls are measured using a contact mode profilometer (Bruker, Dektak XT). The chemical composition of LIG films was investigated using X-ray photoelectron spectroscopy (XPS: Kratos AXIS 165). The Raman spectra were recorded using a Renishaw Raman spectrometer (inVia) using a 532 nm laser source, using a nominal power of 25 mW for 60 s, 50× magnification. The microstructure of the samples was investigated using transmission electron microscopy (TEM, Joel 2100F). A software-controlled needle dosing system (DSA 100E, KRÜSS GmbH) was used for electrowetting and contact angle measurement purposes.

Electrolyte (1M KCl) drops of 4 µl volume and DC bias was applied for the electrowetting experiment. All electrochemical measurements were done using an Autolab 302N potentiostat/galvanostat (Metrohm Autolab BV, Utrecht, The Netherlands) controlled by NOVA software.

3. Results and discussion

Irradiation of CO_2 laser on a commercial polyimide film in ambient air converted the PI film into a porous graphene structure. With software controlled laser writing, LIG can be readily patterned into different morphologies as shown in the SEM images in Figure 1. The appearance of walls and valley-like structures can be seen where walls are predominantly the porous 3D graphene and the valleys in-between the walls are the untreated PI film. The cross-sectional SEM images of LIG film (inset I of Figure 1a) reveal that the height of the walls is ~600 µm. A similar kind of surface morphology is observed for the film LIG_{200} except the wall height is reduced to ~480 µm (inset II of Figure 1b). In the case of PLIG and $PLIG_{200}$, the patterned architecture (Figure S1, supporting information) produced microvoids on top of the LIG walls which results in a high porosity (Figure 1c and d). These air pockets introduce micro-scale surface roughness on the graphene walls, which is combined with nanoscale surface roughness associated with the densely packed vertically aligned graphene fibers. The dual-scale (nano-micro feature) roughness plays a crucial role to control wettability and superhydrophobic stability. After being annealed in the air at 200^{o}C, PLIG microvoid dimensions have slightly reduced as compared to the PLIG (Figure 1f). During the annealing, the induced capillary force due to the loss of moisture will cause the PLIG walls to shrink which in turn reduces the microvoids dimension of $PLIG_{200}$.[34] The SEM image of the PLIG and $PLIG_{200}$ at low magnification is represented in Figure S2. The high magnification SEM images (Figure S3, supporting information) of these films reveal the fiber-like geometry in

which fibers are crosslinked to each other to form a porous graphene structure. A surface profilometer is also used to verify the results obtained from SEM image analysis. Surface variation of LIG, LIG_{200}, PLIG, and $PLIG_{200}$, measured by vertical stylus displacement is presented in Figure S4. The wall height of LIG, LIG_{200}, PLIG, and $PLIG_{200}$ films are found to be ~668, ~520, ~350, and ~236 μm respectively. The height profiles obtained from SEM and surface profilometry methods are matched closely.

Wettability is highly susceptible to surface morphology and surface chemistry, usually determined by an evaluation of the water contact angle (WCA) value. We found that as prepared LIG substrate is hydrophobic (WCA ~111^o) and becomes superhydrophobic (WCA ~153^o) when LIG is air annealed at 200^{o}C for one hour (Figure S5). When microscale roughness is introduced in the LIG substrate by creating microvoids on top of LIG walls, its hydrophobicity is increased (WCA ~128^o) as compared to LIG. After being annealed at 200^{o}C for one hour PLIG becomes superhydrophobic with a WCA value ~151^o, similar to that of LIG_{200}. The superhydrophobic substrates (LIG_{200} and $PLIG_{200}$) are air-stable with no noticeable changes in the WCA value up to 10 min. The droplet eventually evaporates from the films without any obvious sinking in the porous structure. Note that in all LIG surfaces with walls and valley-like structures where suspended drops lie on top of the walls with air pockets beneath them corresponding to the Cassie-Baxter state.[35] Droplet rolling experiment is also performed by tilting the sample substrate. The roll-off angle of droplets on the LIG, LIG_{200}, PLIG, and $PLIG_{200}$ substrates are approximately 23^o, 19^o, 29^o, and 16^o respectively. The roll-off characteristics on the air annealed samples are improved as compared to the pristine LIG and PLIG films. By modulating the surface roughness and surface chemistry via imprinted topography or through air annealing we can tailor the wettability of the LIG films over a wide range as illustrated in Figure S5.

The wetting behavior of the conductive graphene thin films under an external applied electric field is highly relevant for some applications.[36] Figure 2a shows the schematic diagram of

the electrowetting setup, where, a copper wire is inserted into the droplet (1 M KCL) to establish the electrical contact. First, we analyzed the droplet response with graphene substrates acting as the anode (+ve voltage) and copper wire as the cathode (-ve voltage). The droplet shape and the CA response remain unchanged up to 2 V for LIG and PLIG while the value is increased to 3 V for LIG_{200}. Over and above these voltages, an abrupt transition from superhydrophobic Cassie-Baxter (CB) state to superhydrophilic Wenzel (Wn) state is underway and the droplet rapidly sinks in between the graphene fibers. This can be visualized from the snapshots provided in Figure 2c, where droplets sank into the porous structure of LIG, $LIG_{200,}$ and PLIG substrate for a small DC bias of 4, 7, and 5 V respectively. The threshold potential to trigger the droplet transition from CB to Wn state is ~2 V in the case of LIG and PLIG, and 3 V for LIG_{200}. Below this threshold voltage, the CA shows no change with respect to no bias condition and above this, the droplet dynamically penetrates between the graphene fibers causing the CA to be reduced abruptly. Interestingly, for $PLIG_{200}$ substrate the droplet form and CA value at an applied bias of 10 V are almost identical to that at 0 V (Figure 2b). A slow decline in the CA value for $PLIG_{200}$ can be seen for above 10 V bias and the threshold voltage required to activate the sinking of droplets into the air pockets is ~45 V (Figure S6, supporting information), which is nearly 20 times greater than that of other three graphene substrates.

Next, the droplet dynamics are observed in reverse polarity, i.e; graphene substrates as a cathode (-ve voltage) and copper wire as an anode (+ve voltage). The snapshots in Figure 2c show the droplet profiles with the particular applied potential. It is interesting to see that the droplet sinking strongly depends on the polarity of the applied DC bias. In terms of no bias condition, the change in the CA for LIG, $LIG_{200,}$ and PLIG substrate is marginal up to 10 V of applied bias (Figure 2b). A progressive decrease in CA is observed for voltages greater than 10 V (Figure S7 supporting information). The threshold voltage required to allow droplet sinking for LIG, $LIG_{200,}$ and PLIG substrates are 32 V, 44 V, and 33 V respectively, which is

15 times higher than when these substrates act as the anode. Surprisingly, the CA for the $PLIG_{200}$ has changed from 146^{o} to 114^{o} with a relatively small-applied bias of 4 V. Therefore, when LIG, $LIG_{200,}$ and PLIG substrates serve as an anode the CB to Wn transition takes place with the onset of threshold voltage below 5 V, whereas it required more than 30 V when these substrates serve as a cathode. On the other hand, the electrowetting behavior of $PLIG_{200}$ is opposite as compared with the other three substrates. Careful observation of these four electrodes shows there are two separate wetting mode transitions, namely CB to Wn and CB to CB, and the specifics are outlined in Table 1.

Figure 2c also illustrates an interesting application of this electrowetting phenomenon. Considering the panel II of Figure 2c, three different contact angle (152^{o}, 19^{o,} and 139.5^{o}) regions are observed for the no bias, 7 V and -15 V applied bias to the LIG_{200} surface. It is to note, the droplet is no longer sinks into the LIG_{200} surface and sits stably at a contact angle of 19^{o} and 139.5^{o} after DC biases are switched off. Similar types of electrowetting are also observed for LIG, PLIG, and $PLIG_{200}$ surfaces respectively. Polarity dependent electrowetting is, therefore, can modulate the local wettability of any point on these graphene surfaces. It is evident from Figure 2c, an extreme wettability gradient from superhydrophobic to superhydrophilic regions can be engineered on the laser-induced graphene substrates. Such wettability contrast has a wide range of applications which includes, guided fluid transport, fog harvesting, biomedical devices, drug release coatings, and lab-on-chip devices.[37–39]

Figure 3 demonstrates another interesting application of this electrowetting phenomenon. Here we carried out a series of control experiments without the Cu wire to determine whether the Cu wire plays an influential role in the observed voltage polarity dependent electrowetting phenomena. The liquid droplets are sandwiched between the two graphene films for these experiments. In the first series of experiments, the bottom graphene electrodes are acting as an anode and the top ones are acting as the cathode (Figure 3a-d). For LIG, LIG_{200}, and PLIG the droplet is drawn towards the bottom electrode and eventually detached from the cathode

surface at a small DC bias of 2 V. However, for $PLIG_{200}$ (Figure 3d) the liquid droplet is pumped towards the cathode side. During the second series of experiments, the bottom graphene electrodes serve as cathode and the top electrodes serve as the anode (Figure 3e-h). Once again, the liquid droplet is pushed towards the anode side (top electrode) and finally isolated from the bottom electrode at an applied bias of 2 V, 2.5 V, and 4.5 V for LIG, LIG_{200}, and PLIG respectively. For $PLIG_{200}$, the droplet response is opposite to that of the other three electrodes where the droplet is pumped towards the cathode side (lower electrode). Figure 3 displays the directional controlled transport of liquid where the droplet can either be pumped up or down or evenly distributed between the top and bottom electrodes just by altering the applied voltage polarity.

There are many factors, such as surface morphology and roughness, degree of oxidation of the graphene substrates, presence of dangling bonds, induced defects on the graphene surfaces during the lasing process, etc. which can influence the surface energy, and in turn the wettability of the graphene substrates. The voltage polarity dependent electrowetting is another aspect that requires further analysis in terms of identifying the changes in the chemical composition along with the physical changes of these films. Therefore, various spectroscopic, microscopic, and electrochemical tools are used to analyze the material properties to explain the factors responsible for the observed changes in wettability and the subsequent electrowetting performance.

The quality of the graphene films is first evaluated using Raman spectroscopy. From the Raman spectra of Figure 4a, all graphene samples are observed to exhibit the first order fundamental G peak (~1573 cm^{-1}), the D peak (~1340 cm^{-1}) induced by defects on sp^2-bonded carbon, and a 2D peak at around 2670 cm^{-1} induced by 2^{nd} order zone boundary phonons.[40] All Raman spectra analytical processing parameters are summarized in Table S1 (supporting information). The 2D peaks are fitted with only one Lorentzian peak centered ~2675 cm^{-1}, ~2678 cm^{-1}, ~2672 cm^{-1}, ~2665 cm^{-1} with a full width at half maximum (FWHM) value of 80

cm^{-1}, 70 cm^{-1}, 77 cm^{-1}, and 86 cm^{-1} for LIG, LIG_{200}, PLIG, and $PLIG_{200}$ respectively. This type of 2D band profile is the same as observed in a few layers of graphene stacked along the c axis.[41–43] The presence of the D band is an indicator of disorder or defects in the graphene layers and the intensity ratio between D and G band (I_D/I_G) is often used to estimate the amount of defects in graphene-based materials.[44] The I_D/I_G ratio of LIG is calculated as 0.55. Upon annealing at 200°C, the most apparent feature that can be seen is the decrease in the D-band intensity. As a result, the intensity ratio between D and G band (I_D/I_G = 0.47) for LIG_{200} is therefore reduced i.e.; LIG_{200} has low defect concentration relative to the pristine LIG. After being created air pockets on the LIG walls (PLIG), and further annealed at 200°C ($PLIG_{200}$) the D peak intensity increased whereas 2D peak intensity is decreased in comparison with LIG indicating significant structural disorder and defect formation.[45] These induced defects in the graphene substrates could be due to the charge doping or strain.[44] In our findings, however, only a small fluctuation of G band FWHM can be found and there is no 2D band blueshift after annealing or producing microvoids, which suggests that the effect of charge doping can be ignored.[44] The observed Raman outcomes are therefore caused mainly by strain. The effect of compressive strain on the PI sheet due to laser irradiation contributes to a wrinkle-shaped structural disorder, which further increases through the creation of microvoids. Another interesting observation is that the intensity ratio of the 2D to G band is also significantly reduced for PLIG and $PLIG_{200}$, in comparison to LIG and LIG_{200} i.e. the number of ordered graphene layers is reduced too.[46] Further evidence of the formation of wrinkles and the reduction of graphene layers in the case of PLIG and $PLIG_{200}$ is gathered by high-resolution TEM (HRTEM) analysis.

The standard HRTEM images of the graphene films are shown in Figure 4b, which shows the characteristic wrinkles of the graphitized polyimide sheet as reported previously.[41] The signature of the few-layer graphene structure can be seen on the LIG surface (Figure 4b (I)) where disordered fringes are found on the center and ordered graphene fringes are located

near the edge of the fiber respectively. The formation of these wrinkled structures happens due to thermal expansion during laser irradiation.[41] The interlayer spacing of LIG is about 0.37 nm (inset of Figure 4b(I)) which is slightly larger than that of (002) plane of graphite (0.34 nm). This large interlayer spacing of LIG is caused by the presence of the oxygen functional groups or water molecules.[47] For LIG_{200} substrates, both the number of graphene layers near the fiber edges and the interlayer distance (d_{002} = 0.345 nm) are reduced as compared to LIG (Figure 4b(II)). The post-annealing treatment eliminates maximum oxygen functional groups from the LIG surface which results in a reduction of d_{002} value. However, abundant wrinkles are also present on the LIG_{200} surface. On the other hand, HRTEM images of both PLIG and $PLIG_{200}$ also display few-layer features, with an interlayer distance of approximately 0.33 nm (Figure 4b (III) and (IV)). In contrast with LIG and LIG_{200}, the number of ordered PLIG and $PLIG_{200}$ layers is however further decreased. The observed disordered structure in the HRTEM images of PLIG and $PLIG_{200}$ agrees well with the high I_D/I_G ratio seen in their Raman spectra. The systematic decrease in d_{002} because of the removal of oxygen-containing groups and observed disordered structures in the HRTEM images are further verified with the XPS analysis.

XPS is employed to correlate the effect of creating micropattern and post-annealing treatment on the oxygen functionalities and to monitor the structural changes in the graphene substrates. Comparing the carbon/oxygen ratio (C/O) between the four graphene substrates provides an effective way to measure the level of disorder that occurs during patterning or annealing. The atomic C/O ratio is determined (summarized in Table S2, supporting information) by dividing the area under C1s with that of the O1s and multiplying by the photoionization cross-section.[48] A significant disparity of the C/O ratio between LIG and LIG_{200} film is calculated from the XPS survey scan graph (Figure S8, supporting information). The C/O ratio of the pristine LIG is about 16.69, corresponding to 94.35% carbon and 5.65% oxygen content. The C/O ratio increases from 16.69% for LIG to 22.5% and 29.47% for PLIG and LIG_{200}

respectively. This point to an efficient deoxygenation process results in a reduction in d_{002} value for PLIG and LIG_{200} as compared to LIG and these results are consistent with the HRTEM and Raman analysis. However, the air annealed PLIG; i.e., $PLIG_{200}$ has lowered carbon content (94.19%) and improved oxygen content (5.22%) as compared to PLIG giving an overall C/O ratio of ~18. In addition to carbon and oxygen, a small fraction of nitrogen (~0.6%) is also found in PLIG and $PLIG_{200}$ films. The high-resolution C1s XPS spectra of the graphene films showing the dominant C-C peak (~284.3 eV) which indicates that LIG films mainly consist of sp^2 carbon (Figure 4c). In addition to the graphitic carbon, other carbon components (~285.1 eV) corresponds to the diamond-like carbon structure and a residual C-O bond contribution (~286.4 eV) are also present in all graphene films.[49] The extracted binding energy and the contribution of sp^2 carbon and disorder carbon bonding are charted in Table S2. The degree of the defect (i.e.; disordered graphitic carbon or sp^3 carbon) is maximum for the $PLIG_{200}$ surface, whereas LIG_{200} shows the lowest fraction of oxygen-containing groups and the highest fraction of ordered sp^2 carbon. These results are in good agreement with the HRTEM analysis as well.

We also measured the sheet resistance of all graphene substrates using a four-point probe resistivity measurement system (Figure S9, supporting information). These results are similar to that of another recent study on laser-induced graphene fibers.[50] The low sheet resistance confirms there is no dielectric or insulating layer present on the laser-induced graphene fibers.

Apart from all these physical characterizations, we have carried out some electrochemical characterizations (EC impedance spectroscopy, and cyclic voltammetry) in the presence of an electrolyte (1 M KCl) to investigate the charge transfer kinetics and to measure the interfacial capacitance at the electrode-electrolyte interface.

A frequency response analysis of the impedance spectra within the frequency range from 0.1 Hz to 100 kHz yields the Nyquist plot as shown in Figure 5 (a-d). An equivalent electrical circuit was modeled to simulate the capacitive and resistive elements and is represented in the

inset of Figure 5d. These circuit parameters include the solution resistance (R_s: takes care of solution resistance), charge transfer resistance (R_{ct}: arises due to the fast-faradic reaction at the electrode-electrolyte interface), interfacial capacitances (C_{EDL} and C_{air}), and constant phase elements (CPE) which comes due to the nonlinearity and inhomogeneity in the system.[51,52] The fitting results are shown in Table 2. In accordance with the microstructural and surface chemical evolution of graphene samples due to micropatterning and annealing, the charge transfer resistance (R_{ct}) of LIG_{200} is the lowest (20 Ω) as compared to LIG, PLIG, and $PLIG_{200}$ respectively. This is due to the increased density of the delocalized electrons, stimulated from the sp^2 conjugated carbon lattice, which is significantly increased during the annealing process (validated from XPS analysis as well). These increased sp^2 domains provide a low resistant channel for charge transfer within the electrode-electrolyte interface.[53] On the other hand, the contribution of the interfacial capacitance C is composed of two parts, namely, C_{EDL} and C_{air}, which are the electrical double layer (EDL) contribution and the capacitance due to trapped air respectively. Here C_{air} depends on the geometry of the graphene samples whereas, C_{EDL} is strongly affected by the surface chemistry and the applied potential.[51] In our case, the C_{EDL} value is lowest for $PLIG_{200}$ and highest for LIG_{200}. The C_{EDL} value of LIG is however comparable to that of LIG_{200}. Note that, due to the construction of air pockets, the trapped air occupies a large portion of the interfacial area in case of PLIG and $PLIG_{200}$ and contributed significantly to the interfacial capacitance. Interestingly for $PLIG_{200}$ the interfacial capacitance is dominated by the C_{air}. The interfacial capacitance plays a substantial role in the electrowetting behavior of all graphene samples. Therefore, to quantify the value of interfacial capacitance cyclic voltammetry (CV) is performed further.

Figure 5e represents the typical CV behavior of all graphene samples in 1 M KCl at a scan rate of 50 mV s^{-1} within the potential range of 0 to 5 V and the calculated interfacial capacitance values are inserted in the inset of Figure 5e. As shown in Figure 5e(I), LIG

exhibits the maximum current under the CV curve, which corresponds to the maximum interfacial capacitance of 49 mF cm^{-2}. A decrement in the interfacial capacitances is observed for the PLIG, LIG_{200}, and $PLIG_{200}$ samples respectively. It is known that the oxygen-containing groups are capable of providing pseudocapacitance (PC) in the graphene substrates.[54] In our case LIG has the maximum percentage of oxygen-containing groups (responsible for PC), which ultimately maximizes interfacial capacitance of LIG. For LIG_{200} most of the PC part is eliminated due to the removal of PC-active oxygen functional groups at 200^{o}C and the result is consistent with the XPS analysis.

Based on the above experimental results we can say that LIG surface hydrophobicity is modulated by both surface morphology and surface chemistry. Both of these considerations need to take into account when analyzing the graphene specimens as changes in surface chemistry are often associated with the changes in the surface morphology.[24] First consider the effect of morphology, porosity, and roughness on the wettability properties of graphene substrates. Note that for the LIG surface, the suspended drops lie on the top of the walls with air beneath them which corresponding to the Cassie-Baxter state.[35] The traditional concept of roughness dependent wettability models (Wenzel and Cassie-Baxter) leads to the fact that a hydrophilic surface becomes more hydrophilic and a hydrophobic surface becomes more hydrophobic with the increase in the surface roughness.[35,55] The SEM results indicate that building microvoids on the LIG walls (PLIG) creates sufficient hierarchical surface roughness which causes a large volume of trapped air between the miro-nanoscale surface cavities, resulting in a composite solid-air-liquid interface. This hierarchical dual scale (micro-nano) roughness improves the PLIG hydrophobicity (WCA ~128^{o}) as compared to LIG (WCA ~110^{o}).[27] However, the superhydrophobicity of LIG_{200} (WCA ~152^{o}) cannot be clarified by considering the CB model only, as surface topography of LIG_{200} is similar to that of LIG (see Figure 1). Now, let's consider the changes in their surface chemical states. It is well known that sp^2 rich surfaces minimize the surface energy and raising the carbon film

hydrophobicity.[28] XPS analysis confirmed that LIG_{200} possesses a maximum percentage of sp^2 hybridized carbon, which is responsible for the enhancement in the hydrophobic nature of the LIG_{200} substrate. Literature also suggests that graphene samples with low oxygen content or less oxygen functionalities (C-O, C=O) always have a higher CA. This relation is simplified by the fact that the bonds between C-O and C=O are more polar than the bonds of C-C or C-H so that more oxygen content at the graphene edges are more likely to interact with water, thus more hydrophilic.[24] The outcome of XPS shows that oxygen levels are nearly halved in air-annealed LIG relative to pristine LIG and thus we observe a higher CA for LIG_{200} (~152^o). The superhydrophobicity of LIG_{200} is therefore supported by the fact of the high fraction of sp^2 carbon and a low percentage of oxygen functional groups. Surprisingly, despite a slight increase in oxygen content and a decrease in sp^2 carbon compared to PLIG, air annealed PLIG ($PLIG_{200}$) results in a superhydrophobic surface(~151^o). It has been noted that graphene hydrophobicity is also appeared due to the basal planes, whereas edge planes contribute hydrophilicity.[24] We believed that air annealing maximizes the exposure of graphene basal planes in both LIG_{200} and $PLIG_{200}$, resulting in superhydrophobic surfaces.

Next, by submitting the graphene surfaces to electrowetting, a complete or incomplete transition from a state of superhydrophobic CB to superhydrophilic Wn state is systematically achieved (Table 1). To explain the voltage polarity dependent electrowetting results, we first considered classical electrowetting phenomena. In general, electrowetting is independent of the applied voltage polarity. The CA change with voltage is symmetrical for both positive and negative bias, according to the Young-Lippmann (YL) model (equation 1).[4]

$$\boldsymbol{Cos\theta = Cos\theta_o + \frac{CV^2}{2\gamma_{LV}}} \quad \text{.....1}$$

Where, θ_o and θ is the CA without and with applied bias, γ_{LV} is the interfacial tension and C is the interfacial capacitance. YL model, therefore, does not seem to clarify the abrupt transition from non-wetting to wetting state at low voltages when the graphene substrates

(LIG, PLIG, LIG_{200}) are acting as an anode. To describe the voltage polarity dependent irreversible electrowetting, we take into account the role of water electrolysis.[27,28,51] The water electrolysis directs hydrogen ion (H^+) toward Cu electrode during +ve potential applied to graphene films, whereas liquid-solid (graphene) interfaces attract hydroxyl ions (OH^-). Since there are more oxygen reactive groups in LIG and PLIG as compared to LIG_{200}, their oxidation resistance is lower than LIG_{200}. Therefore, the electrochemical oxidation at positive applied potential improves their wettability further and a faster CA fall was observed (see Figure 2b). When these films are acting as the cathode, no further oxidation took place and the oxidized portions are wetted only while the major portions of these films still nonwetted to the water droplet. The DC biases can thus be used to wet the graphene surfaces (LIG, PLIG, LIG_{200}) in a controllable way. In fact, water transport through these surfaces can be stopped and then restart again on request according to the voltage applied, as represented in Figure 3.

To confirm our hypothesis we performed a simple test. First, we wetted the LIG_{200} by the application of voltage. After 2 mins we put a 2^{nd} droplet without any voltage being applied. Because of the electrochemical oxidation of the LIG_{200}, the 2^{nd} droplet also wetted the surface. We observed that the hydrophobicity of the LIG_{200} surface is restored partially (contact angle ~ 130^o) upon vacuum annealing it at 250^oC because oxygens are desorbed with high-temperature treatment.

Surprisingly, despite having a significant amount of oxygenated groups, the voltage polarity dependent electrowetting for $PLIG_{200}$ is opposite from that observed for the other three substrates. This strange electrowetting behavior of $PLIG_{200}$ can be correlated with its hierarchical micro and nanoscale surface roughness. It is reported that patterned surfaces with dual scale roughness (micro-nano) are ideal to improve their superhydrophobic stability compared to uniform ones.[56] In contrast to LIG and LIG_{200}, the presence of microscale roughness with large air pockets prevents CB to Wn transition with a small positive applied bias to the $PLIG_{200}$. The existence of large air pockets of the $PLIG_{200}$ substrate reduces the

interfacial contact area between solid and liquid which in turn increases the contact resistance. A much higher electrical bias is therefore required to produce enough electric charges at the interfaces between $PLIG_{200}$ and droplet to impact the CB to Wn transition as demonstrated in Figure S6.

It is interesting to note that the electrowetting behavior of PLIG and $PLIG_{200}$ is opposite despite having a similar kind of hierarchical surface roughness. This can be explained by taking into account the role of interfacial capacitance. According to the YL equation (Eq. 1), interfacial capacitance is also an influencing factor to control the polarity dependent electrowetting phenomena.[51] In the present case, the equilibrium interfacial capacitance C consists of two parts, namely C_{EDL} (electrical double layer) and C_{air} (capacitance due to trapped air). Where the value of C_{air} is dependent on the geometry of the film and C_{EDL} is strongly affected by both the ionic concentration and the applied potential.[51],[57] The LIG, PLIG, and LIG_{200} possess a high C_{EDL} value (in μF range, see table 2). Very strong electrowetting effects are therefore regulated by C_{EDL} when LIG, PLIG, and LIG_{200} acting as the anode.[51] But the introduction of micron size air pockets led to a huge decrease in the C_{EDL} (see table 2) for $PLIG_{200}$. The feeble C_{EDL} therefore weakly affects the electrowetting when $PLIG_{200}$ served as anode whereas the significant contribution of C_{air} may be responsible for the powerful impact on electrowetting effect when $PLIG_{200}$ served as the cathode. According to equation 1, a relatively high interfacial capacitance can cause a much faster CA change with respect to the applied voltage.[27] For the pristine LIG film in the CB state, shows high interfacial capacitance (~49 mF cm^{-2} as evaluated from the CV analysis) which led to the strong electrowetting effect. The interfacial capacitance values of PLIG and LIG_{200} are almost identical, resulting in a similar kind of electrowetting behavior. Whereas very low interfacial capacitance (~1 mF cm^{-2}) led to a relatively weak electrowetting effect for the $PLIG_{200}$ substrate.

4. Conclusion

In conclusion, we have demonstrated the voltage polarity dependent directionally controlled transport of liquid through the laser-induced graphene surface, where a threshold bias is required to activate the transport. The strong voltage polarity dependent wetting of LIG, PLIG, and LIG_{200} suggests that the attached oxygen-containing functional groups and high interfacial capacitance (C_{EDL}) causes the observed transition from nonwetting to wetting state when these films are acting as the anode. Whereas, the unique architecture of $PLIG_{200}$ which combines both micro and a nanoscale surface topology delays the onset of CB to Wn transition as compared to LIG, PLIG, and LIG_{200} anode. Interestingly, water can efficiently wet $PLIG_{200}$ cathode with the application of a slight DC bias of 4 V due to the low interfacial capacitance which is dominated by C_{air} only. Finally, the controllable pumping of water between the graphene surfaces that we demonstrated here could have strong applications in the biomedical field, lab-on-chip devices, nanofluidic plumbing systems, microfluidic channels where control movement of liquid is required with great precision.

Acknowledgments

Dr. S. Deshmukh and Dr. P. R. Waghmare thank the Natural Science and Engineering Research
Council (NSERC) for the financial support in the form of Grant No. RGPIN-2015-06542.

References

[1] M.E. Suk, N.R. Aluru, Water Transport through Ultrathin Graphene, J. Phys. Chem. Lett. 1 (2010) 1590–1594.

[2] Z. Wang, L. Ci, L. Chen, S. Nayak, P.M. Ajayan, N. Koratkar, Polarity-Dependent Electrochemically Controlled Transport of Water through Carbon Nanotube Membranes, Nano Lett. 7 (2007) 697–702.

[3] J. Rafiee, M.A. Rafiee, Z.-Z. Yu, N. Koratkar, Superhydrophobic to Superhydrophilic Wetting Control in Graphene Films, Adv. Mater. 22 (2010) 2151–2154.

[4] F. Mugele, J.-C. Baret, Electrowetting: from basics to applications, J. Phys. Condens.

Matter. 17 (2005) R705–R774.

[5] B. Kakade, R. Mehta, A. Durge, S. Kulkarni, V. Pillai, Electric Field Induced, Superhydrophobic to Superhydrophilic Switching in Multiwalled Carbon Nanotube Papers, Nano Lett. 8 (2008) 2693–2696.

[6] J. Li, N.S. Ha, T. 'Leo' Liu, R.M. van Dam, C.-J. 'CJ' Kim, Ionic-surfactant-mediated electro-dewetting for digital microfluidics, Nature. 572 (2019) 507–510.

[7] R.A. Hayes, B.J. Feenstra, Video-speed electronic paper based on electrowetting, Nature. 425 (2003) 383–385.

[8] P.Y. Keng, S. Chen, H. Ding, S. Sadeghi, G.J. Shah, A. Dooraghi, M.E. Phelps, N. Satyamurthy, A.F. Chatziioannou, C.-J. "CJ" Kim, R.M. van Dam, Micro-chemical synthesis of molecular probes on an electronic microfluidic device, Proc. Natl. Acad. Sci. 109 (2012) 690 LP – 695.

[9] V. Srinivasan, V.K. Pamula, R.B. Fair, An integrated digital microfluidic lab-on-a-chip for clinical diagnostics on human physiological fluids, Lab Chip. 4 (2004) 310–315.

[10] B. Berge, J. Peseux, Variable focal lens controlled by an external voltage: An application of electrowetting, Eur. Phys. J. E. 3 (2000) 159–163.

[11] A.A. Balandin, S. Ghosh, W. Bao, I. Calizo, D. Teweldebrhan, F. Miao, C.N. Lau, Superior Thermal Conductivity of Single-Layer Graphene, Nano Lett. 8 (2008) 902–907.

[12] Y. Zhang, Y.-W. Tan, H.L. Stormer, P. Kim, Experimental observation of the quantum Hall effect and Berry's phase in graphene, Nature. 438 (2005) 201–204.

[13] K.S. Novoselov, A.K. Geim, S. V Morozov, D. Jiang, M.I. Katsnelson, I. V Grigorieva, S. V Dubonos, A.A. Firsov, Two-dimensional gas of massless Dirac fermions in graphene, Nature. 438 (2005) 197–200.

[14] K.S. Novoselov, A.K. Geim, S. V Morozov, D. Jiang, Y. Zhang, S. V Dubonos, I. V Grigorieva, A.A. Firsov, Electric Field Effect in Atomically Thin Carbon Films, Science (80-.). 306 (2004) 666 LP – 669.

[15] H. Hu, Z. Zhao, Y. Gogotsi, J. Qiu, Compressible Carbon Nanotube–Graphene Hybrid Aerogels with Superhydrophobicity and Superoleophilicity for Oil Sorption, Environ. Sci. Technol. Lett. 1 (2014) 214–220.

[16] X. Dong, J. Chen, Y. Ma, J. Wang, M.B. Chan-Park, X. Liu, L. Wang, W. Huang, P. Chen, Superhydrophobic and superoleophilic hybrid foam of graphene and carbon nanotube for selective removal of oils or organic solvents from the surface of water, Chem. Commun. 48 (2012) 10660–10662.

[17] Y. Lin, G.J. Ehlert, C. Bukowsky, H.A. Sodano, Superhydrophobic Functionalized Graphene Aerogels, ACS Appl. Mater. Interfaces. 3 (2011) 2200–2203.

[18] R. Li, C. Chen, J. Li, L. Xu, G. Xiao, D. Yan, A facile approach to superhydrophobic and superoleophilic graphene/polymer aerogels, J. Mater. Chem. A. 2 (2014) 3057–3064.

[19] E. Singh, Z. Chen, F. Houshmand, W. Ren, Y. Peles, H.-M. Cheng, N. Koratkar, Superhydrophobic Graphene Foams, Small. 9 (2013) 75–80.

[20] L. Li, J. Zhang, Z. Peng, Y. Li, C. Gao, Y. Ji, R. Ye, N.D. Kim, Q. Zhong, Y. Yang, H. Fei, G. Ruan, J.M. Tour, High-Performance Pseudocapacitive Microsupercapacitors from Laser-Induced Graphene, Adv. Mater. 28 (2016) 838–845.

[21] P. Nayak, N. Kurra, C. Xia, H.N. Alshareef, Highly Efficient Laser Scribed Graphene Electrodes for On-Chip Electrochemical Sensing Applications, Adv. Electron. Mater. 2 (2016) 1600185.

[22] J. Zhang, C. Zhang, J. Sha, H. Fei, Y. Li, J.M. Tour, Efficient Water-Splitting Electrodes Based on Laser-Induced Graphene, ACS Appl. Mater. Interfaces. 9 (2017) 26840–26847.

[23] C. Zhang, Y. Xie, H. Deng, T. Tumlin, C. Zhang, J.W. Su, P. Yu, J. Lin, Monolithic and Flexible ZnS/SnO2 Ultraviolet Photodetectors with Lateral Graphene Electrodes, Small. 13 (2017) 1604197.

[24] Y. Li, D.X. Luong, J. Zhang, Y.R. Tarkunde, C. Kittrell, F. Sargunaraj, Y. Ji, C.J. Arnusch, J.M. Tour, Laser-Induced Graphene in Controlled Atmospheres: From Superhydrophilic to Superhydrophobic Surfaces, Adv. Mater. 29 (2017) 1700496.

[25] C.M. Tittle, D. Yilman, M.A. Pope, C.J. Backhouse, Robust Superhydrophobic Laser-Induced Graphene for Desalination Applications, Adv. Mater. Technol. 3 (2018) 1700207.

[26] J. Zhang, M. Ren, Y. Li, J.M. Tour, In Situ Synthesis of Efficient Water Oxidation Catalysts in Laser-Induced Graphene, ACS Energy Lett. 3 (2018) 677–683.

[27] J. Pu, S. Wan, Z. Lu, G. Zhang, L. Wang, X. Zhang, Q. Xue, Controlled water adhesion and electrowetting of conducting hydrophobic graphene/carbon nanotubes composite films on engineering materials, J. Mater. Chem. A. 1 (2013) 1254–1260.

[28] S. Deshmukh, K.J. Sankaran, D. Banerjee, C.J. Yeh, K.C. Leou, D.M. Phase, M. Gupta, I.N. Lin, K. Haenen, S.S. Roy, P.R. Waghmare, Direct synthesis of electrowettable nanostructured hybrid diamond, J. Mater. Chem. A. 7 (2019) 19026–19036.

[29] D.J. Lomax, P. Kant, A.T. Williams, H. V Patten, Y. Zou, A. Juel, R.A.W. Dryfe, Ultra-low voltage electrowetting using graphite surfaces, Soft Matter. 12 (2016) 8798–8804.

[30] G. Zhang, M. Walker, P.R. Unwin, Low-Voltage Voltammetric Electrowetting of Graphite Surfaces by Ion Intercalation/Deintercalation, Langmuir. 32 (2016) 7476–7484.

[31] K. Ounnunkad, H. V Patten, M. Velický, A.K. Farquhar, P.A. Brooksby, A.J. Downard, R.A.W. Dryfe, Electrowetting on conductors: anatomy of the phenomenon, Faraday Discuss. 199 (2017) 49–61.

[32] Z. Wang, C. Lopez, A. Hirsa, N. Koratkar, Impact dynamics and rebound of water droplets on superhydrophobic carbon nanotube arrays, Appl. Phys. Lett. 91 (2007) 23105.

[33] Y. Qin, X. Wang, Z.L. Wang, Microfibre–nanowire hybrid structure for energy scavenging, Nature. 451 (2008) 809.

[34] Z. Dong, C. Jiang, H. Cheng, Y. Zhao, G. Shi, L. Jiang, L. Qu, Facile Fabrication of Light, Flexible and Multifunctional Graphene Fibers, Adv. Mater. 24 (2012) 1856–1861.

[35] A.B.D. Cassie, S. Baxter, Wettability of porous surfaces, Trans. Faraday Soc. 40 (1944) 546–551.

[36] L. Chen, E. Bonaccurso, Electrowetting — From statics to dynamics, Adv. Colloid Interface Sci. 210 (2014) 2–12.

[37] R.K. Upadhyay, P.R. Waghmare, Green preparation of copper surfaces with wettability contrast for guided fluid transport and fog harvesting application, Mater. Lett. 246 (2019) 223–226.

[38] Y. Lai, L. Lin, F. Pan, J. Huang, R. Song, Y. Huang, C. Lin, H. Fuchs, L. Chi, Bioinspired Patterning with Extreme Wettability Contrast on TiO2 Nanotube Array Surface: A Versatile Platform for Biomedical Applications, Small. 9 (2013) 2945–2953.

[39] L. Zhai, M.C. Berg, F.Ç. Cebeci, Y. Kim, J.M. Milwid, M.F. Rubner, R.E. Cohen, Patterned Superhydrophobic Surfaces: Toward a Synthetic Mimic of the Namib Desert Beetle, Nano Lett. 6 (2006) 1213–1217.

[40] A.C. Ferrari, J.C. Meyer, V. Scardaci, C. Casiraghi, M. Lazzeri, F. Mauri, S. Piscanec, D. Jiang, K.S. Novoselov, S. Roth, A.K. Geim, Raman Spectrum of Graphene and Graphene Layers, Phys. Rev. Lett. 97 (2006) 187401.

[41] J. Lin, Z. Peng, Y. Liu, F. Ruiz-Zepeda, R. Ye, E.L.G. Samuel, M.J. Yacaman, B.I. Yakobson, J.M. Tour, Laser-induced porous graphene films from commercial polymers, Nat. Commun. 5 (2014) 5714.

[42] L.G. Cançado, M.A. Pimenta, R. Saito, A. Jorio, L.O. Ladeira, A. Grueneis, A.G. Souza-Filho, G. Dresselhaus, M.S. Dresselhaus, Stokes and anti-Stokes double resonance Raman scattering in two-dimensional graphite, Phys. Rev. B. 66 (2002) 35415.

[43] M.A. Pimenta, G. Dresselhaus, M.S. Dresselhaus, L.G. Cançado, A. Jorio, R. Saito, Studying disorder in graphite-based systems by Raman spectroscopy, Phys. Chem. Chem. Phys. 9 (2007) 1276–1290.

[44] Z.H. Ni, H.M. Wang, Y. Ma, J. Kasim, Y.H. Wu, Z.X. Shen, Tunable Stress and Controlled Thickness Modification in Graphene by Annealing, ACS Nano. 2 (2008) 1033–1039.

[45] S.P. Surwade, S.N. Smirnov, I. V Vlassiouk, R.R. Unocic, G.M. Veith, S. Dai, S.M. Mahurin, Water desalination using nanoporous single-layer graphene, Nat. Nanotechnol. 10 (2015) 459–464.

[46] A. Das, B. Chakraborty, A.K. Sood, Raman spectroscopy of graphene on different substrates and influence of defects, Bull. Mater. Sci. 31 (2008) 579–584.

[47] S. Indrawirawan, H. Sun, X. Duan, S. Wang, Low temperature combustion synthesis of nitrogen-doped graphene for metal-free catalytic oxidation, J. Mater. Chem. A. 3 (2015) 3432–3440.

[48] P.-G. Ren, D.-X. Yan, X. Ji, T. Chen, Z.-M. Li, Temperature dependence of graphene oxide reduced by hydrazine hydrate, Nanotechnology. 22 (2010) 55705.

[49] P. Zhao, G. Bhattacharya, S.J. Fishlock, J.G.M. Guy, A. Kumar, C. Tsonos, Z. Yu, S. Raj, J.A. McLaughlin, J. Luo, N. Soin, Replacing the metal electrodes in triboelectric nanogenerators: High-performance laser-induced graphene electrodes, Nano Energy. 75 (2020) 104958.

[50] L.X. Duy, Z. Peng, Y. Li, J. Zhang, Y. Ji, J.M. Tour, Laser-induced graphene fibers, Carbon N. Y. 126 (2018) 472–479.

[51] Z. Han, B. Tay, C. Tan, M. Shakerzadeh, K. (Ken) Ostrikov, Electrowetting Control of Cassie-to-Wenzel Transitions in Superhydrophobic Carbon Nanotube-Based Nanocomposites, ACS Nano. 3 (2009) 3031–3036.

[52] D. Banerjee, K.J. Sankaran, S. Deshmukh, M. Ficek, G. Bhattacharya, J. Ryl, D.M. Phase, M. Gupta, R. Bogdanowicz, I.N. Lin, A. Kanjilal, K. Haenen, S.S. Roy, 3D

Hierarchical Boron-Doped Diamond-Multilayered Graphene Nanowalls as an Efficient Supercapacitor Electrode, J. Phys. Chem. C. 123 (2019) 15458–15466.

[53] C.-M. Chen, Q. Zhang, M.-G. Yang, C.-H. Huang, Y.-G. Yang, M.-Z. Wang, Structural evolution during annealing of thermally reduced graphene nanosheets for application in supercapacitors, Carbon N. Y. 50 (2012) 3572–3584.

[54] Y. Zhu, X. Li, Q. Cai, Z. Sun, G. Casillas, M. Jose-Yacaman, R. Verduzco, J.M. Tour, Quantitative Analysis of Structure and Bandgap Changes in Graphene Oxide Nanoribbons during Thermal Annealing, J. Am. Chem. Soc. 134 (2012) 11774–11780.

[55] R.N. Wenzel, RESISTANCE OF SOLID SURFACES TO WETTING BY WATER, Ind. Eng. Chem. 28 (1936) 988–994.

[56] Z. Wang, N. Koratkar, L. Ci, P.M. Ajayan, Combined micro-/nanoscale surface roughness for enhanced hydrophobic stability in carbon nanotube arrays, Appl. Phys. Lett. 90 (2007) 143117.

[57] Z.J. Han, R. Morrow, B.K. Tay, D. McKenzie, Time-dependent electrical double layer with blocking electrode, Appl. Phys. Lett. 94 (2009) 43118.

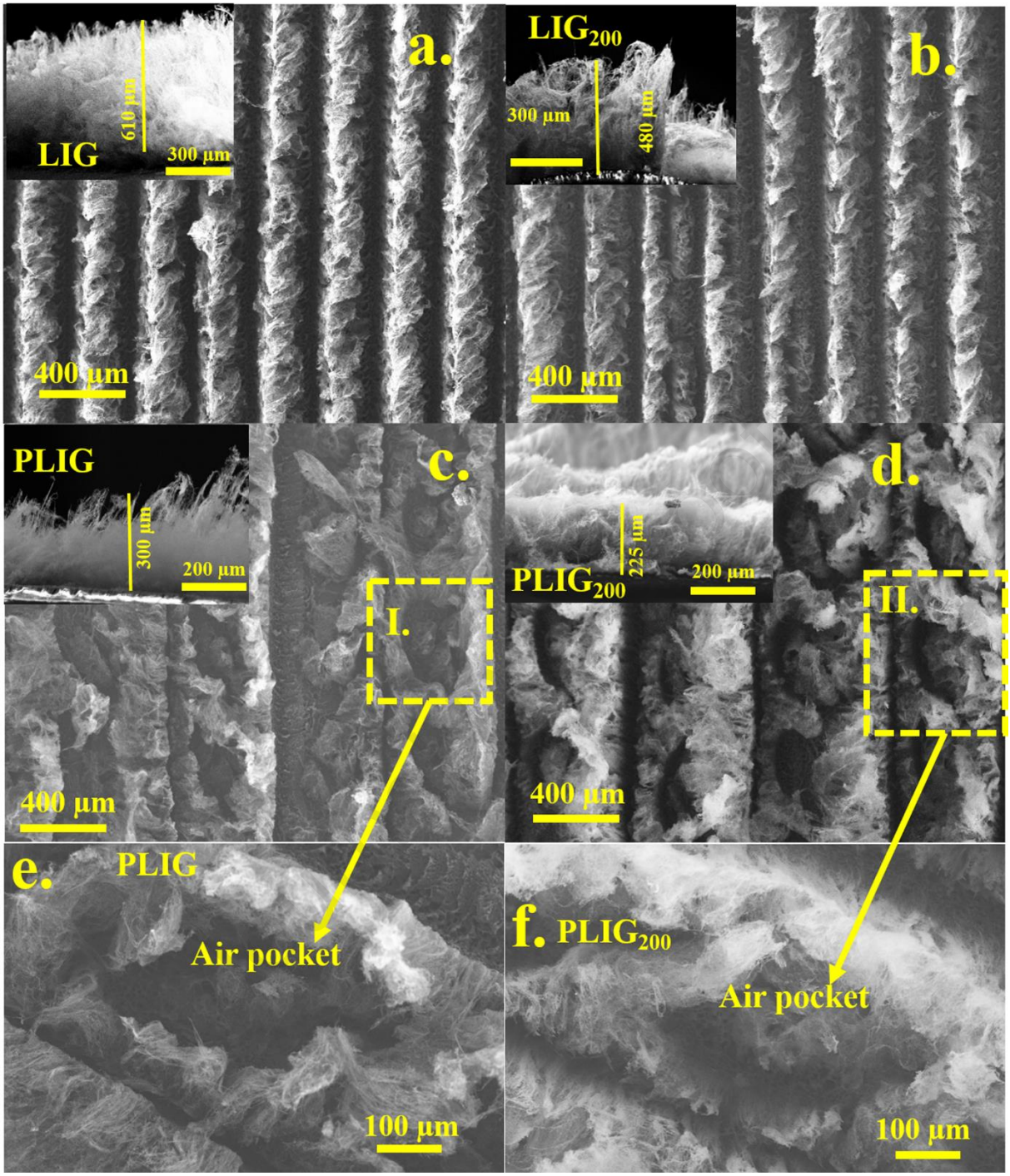

Figure 1. SEM images of (a) LIG (b) LIG_{200} (c) PLIG and (d) $PLIG_{200}$ with insets showing their cross-sectional profile. (e and f) Magnified view of air pockets of PLIG and $PLIG_{200}$ corresponding to the region I and II in Figures 1c and d respectively.

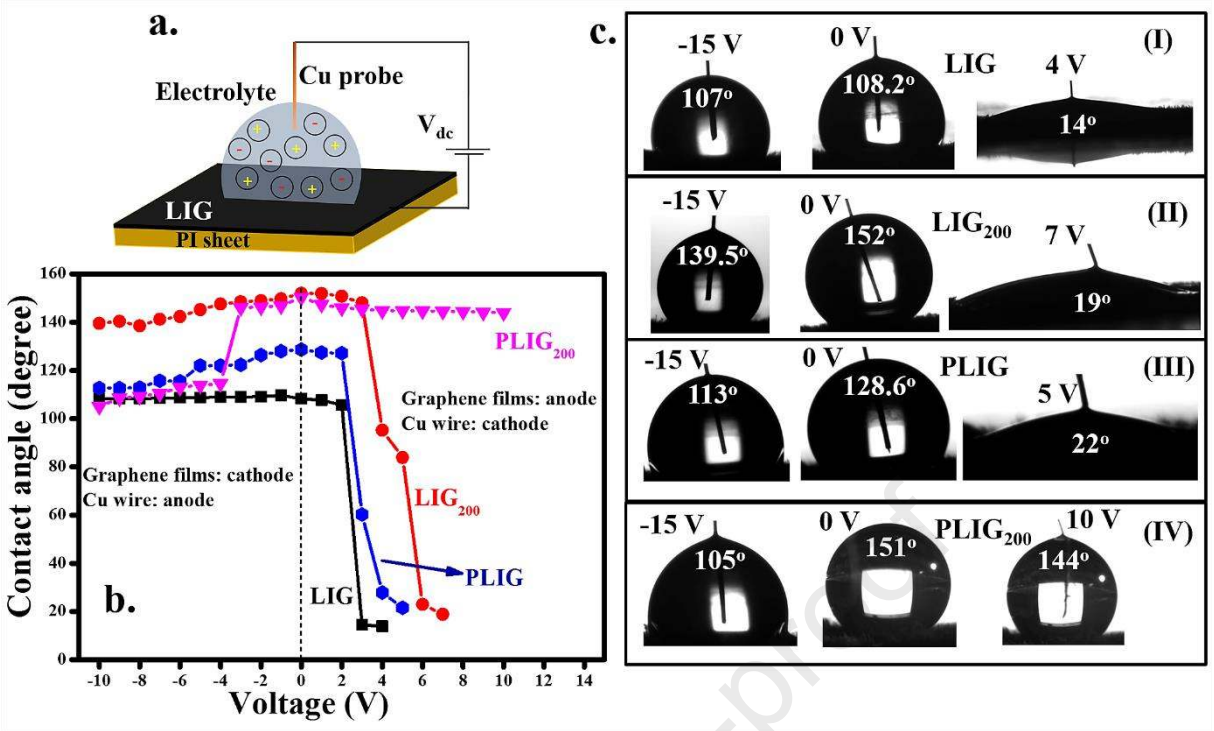

Figure 2. (a) Schematic of the electrowetting experimental setup. (b) Contact angle variation with positive and negative bias applied to the LIG, PLIG, $LIG_{200,}$ and $PLIG_{200}$ electrodes. (c) panels (I-IV) display the snapshots of water droplets on LIG, LIG_{200}, PLIG, and $PLIG_{200}$ electrodes at a particular applied DC bias.

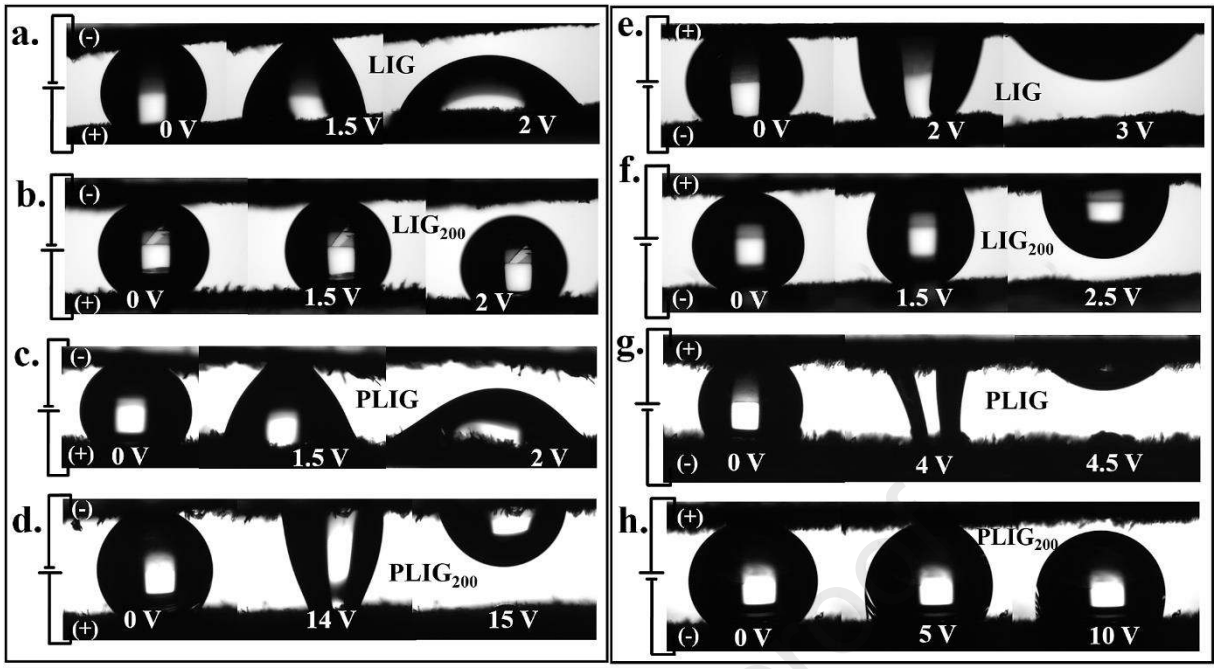

Figure 3. Droplet response with LIG, LIG_{200}, PLIG, and $PLIG_{200}$ electrode as both anode and cathode. Panels (a-d) the bottom electrodes are the anode and the upper electrodes are the cathode, (e-h) the bottom electrodes are the cathode and the upper electrodes are the anode.

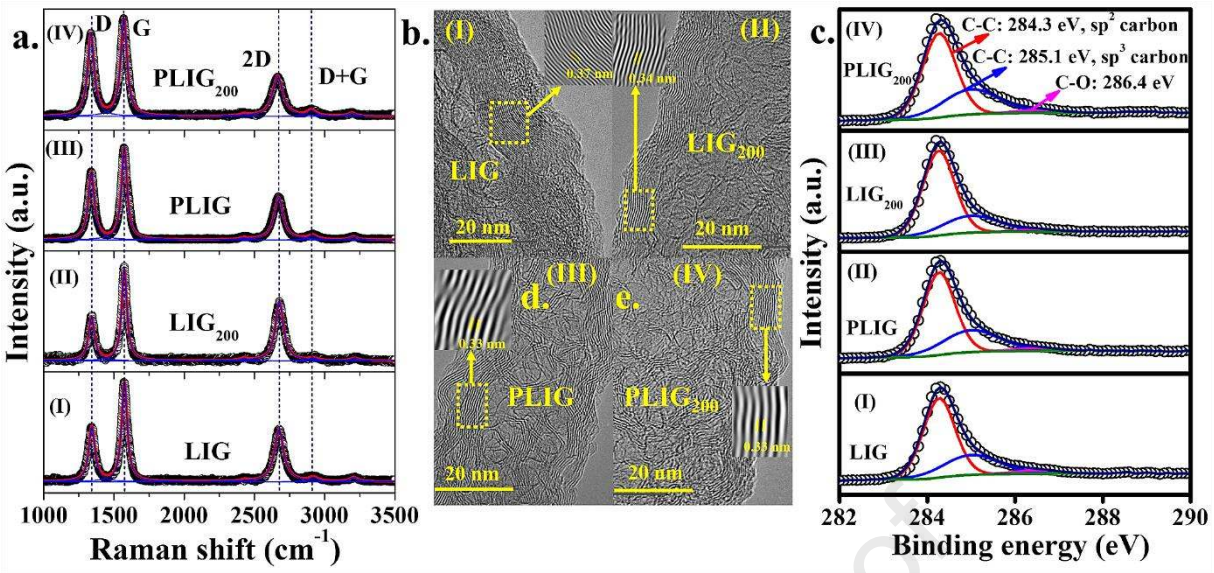

Figure 4. (a) Raman spectra of (I) LIG (II) LIG_{200} (III) PLIG and (IV) $PLIG_{200}$. The open black circles are the experimental data and the solid lines are the fitted curves. (b) HR-TEM images of (I) LIG (II) LIG_{200} (III) PLIG and (IV) $PLIG_{200}$ respectively, with insets showing the inverse FET image of the regions marked in the yellow rectangle. (c) High-resolution C1s XPS spectra of (I) LIG (II) PLIG, (III) $LIG_{200,}$ and (IV) $PLIG_{200}$ surface. XPS spectra showing the dominant C-C (sp^2 hybridized carbon ~284.3 eV) and C-C (sp^3 hybridized carbon ~285 eV) peak.

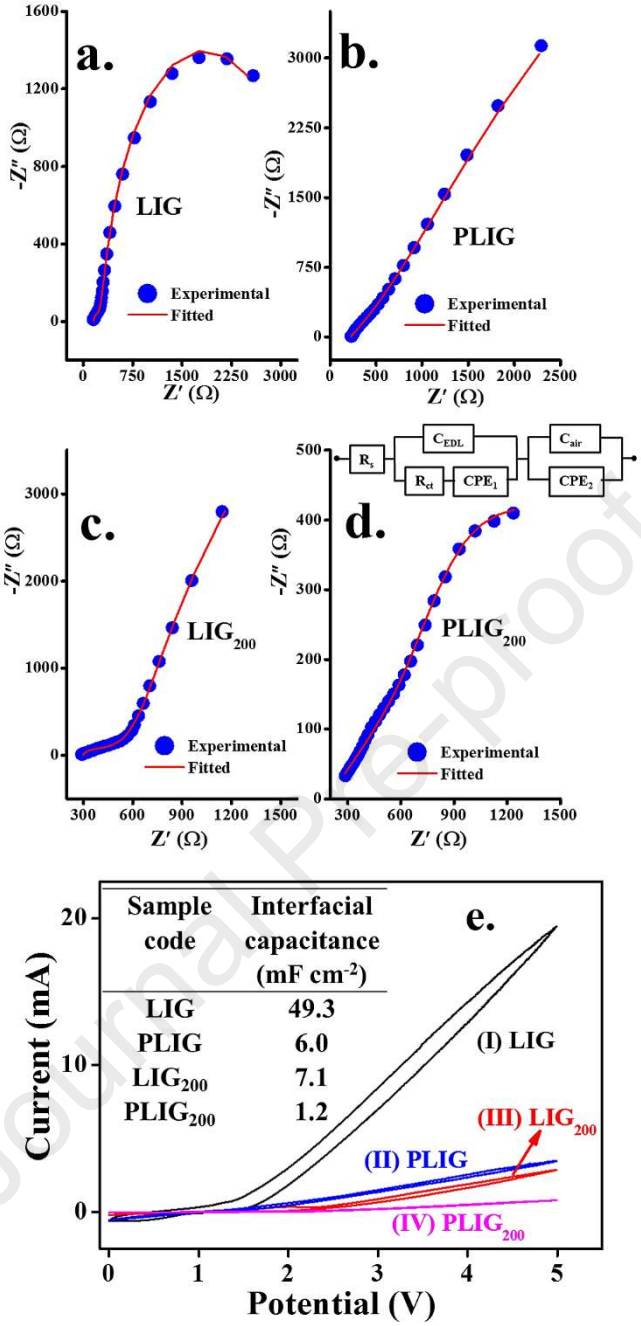

Figure 5. Experimental and fitted impedance spectra of (a) LIG (b) PLIG (c) LIG_{200} and (d) $PLIG_{200}$ electrode. (e) Cyclic voltammetry graphs of (I) LIG (II) PLIG (III) LIG_{200} and (IV) $PLIG_{200}$ electrode. All electrochemical experiments are carried out in 1M KCl aqueous solution.

Table 1. Electrowetting results of graphene electrodes.

Sample code	CA_0	CA_{+VE}	ΔCA_{+VE}	CA_{-VE}	ΔCA_{-VE}
LIG	108.2	14 (CB → Wn) at 4V	94.2	107 (CB → CB) at 15V	1.2
LIG_{200}	152	19 (CB → Wn) at 7V	133	139.5 (CB → CB) at 15V	12.5
PLIG	128.6	22 (CB → Wn) at 5V	106.6	113 (CB → CB+Wn) at 15V	15.6
$PLIG_{200}$	151	144 (CB → CB) at 10V	7	105 (CB → CB +Wn) at 15V	46

CA_0: contact angle at no bias condition; CA_{+VE} and ΔCA_{+VE}: contact angle and change in contact angle at a particular positive applied bias (wetting transition); CA_{-VE} and ΔCA_{-VE}: contact angle and change in contact angle at a particular negative applied bias (wetting transition).

Table 2. EIS circuit parameters of graphene electrodes obtained from equivalent circuit model.

Sample code	R_s	R_{ct}	C_{EDL}	CPE_1	C_{air}	CPE_2
LIG	157 Ω	~ 31 Ω	57.1 µF	5.26 mMho N = 0.323	2.16 mF	5.26 µMho N = 0.041
PLIG	161 Ω	~ 60 Ω	0.276 µF	1.70 mMho N = 0.52	11.9 mF	220 µMho N = 0.01
LIG_{200}	297 Ω	~ 10 Ω	73.4 µF	3.10 mMho N = 0.24	4.30 mF	55.3 µMho N = 0.07
$PLIG_{200}$	150 Ω	~ 35 Ω	10 pF	1.30 mMho N = 0.225	4.50 mF	4.20 µMho N = 0.01

Declaration of interests

☒ The authors declare that they have no known competing financial interests or personal relationships that could have appeared to influence the work reported in this paper.

☐The authors declare the following financial interests/personal relationships which may be considered as potential competing interests: